Electrowetting and droplet impalement experiments on superhydrophobic multiscale structures

F. Lapierre,[a] P. Brunet,[a] Y. Coffinier,[ba] V. Thomy,[a] R. Blossey[b] and R. Boukherroub[ba]

Received 4th December 2009, Accepted 13th January 2010
First published as an Advance Article on the web ?????
DOI: 10.1039/b925544c

The reversible actuation of droplets on superhydrophobic surfaces under ambient conditions is currently an important field of research due to its potential applicability in microfluidic lab-on-a-chip devices. We have recently shown that Si-nanowire (NW) surfaces allow for reversible actuation provided that the surface structures show certain characteristics. In particular it appears that, for such surfaces, the presence of structures with multiple specific length scales is indeed needed to have a robust reversibility of contact angle changes. Here we report on electrowetting (EW) and impalement experiments on double-scale structured surfaces prepared by a combination of silicon micropillars prepared by an association of optical lithography and silicon etching, and nanowire growth on top of these surfaces. We show that while micropillar surfaces have a low impalement threshold and irreversible EW behaviour, a surface with double-scale texture can show both a very high resistance to impalement and a limited reversibility under EW, provided that the roughness of the micro-scale is large enough - *i.e.* that the pillars are tall enough. The optimal performance is obtained for a space between pillars that is comparable to the height of the nanostructure.

I. Introduction

The superhydrophobic character of a surface generally arises from an interplay between the surface roughness and its chemical composition. Seminal contributions to an understanding of such surfaces already date to long ago by Adam,[1] and later on formalised by Cassie and Baxter[2] for the situation of a composite interface. Alternatively, Wenzel's approach addresses the state of homogeneous wetting.[3] The recent upsurge of interest in the subject is driven by the development of more and more sophisticated techniques for the production of surface micro- and nanostructures, which make it possible to mimic water-repellent biosurfaces such as Lotus leaves. Such surfaces have already found numerous applications such as textiles, roof and window coatings, coatings in household materials, microelectromechnical systems (MEMS), or lab-on-a-chip (LOC) devices.[4–7]

In order to control the contact angle, electrowetting[8] has emerged as a versatile technique with a number of microsystems being at the stage of commercialization, *e.g.* adjustable lenses[9] or electronic displays.[10] The state of the field from both theoretical and applied aspects has recently been reviewed by Mugele and Baret.[11] For

[a]*Institut d'Electronique, de Microélectronique et de Nanotechnologies (IEMN), UMR CNRS 8520, F-59652, Villeneuve d'Ascq, France*
[b]*Interdisciplinary Research Institute (IRI), USR CNRS 3078, 50 Avenue Halley, F-59658 Villeneuve d'Ascq, France*

lab-on-a-chip systems and their requirement of low contamination or material loss, electrowetting on superhydrophobic substrates has attracted recent interest.[7,12–15] While electrowetting on planar hydrophobic surfaces is usually reversible under ambient conditions, *i.e.*, the contact angle changes back to its original value once the applied voltage is turned off, most published results on superhydrophobic surfaces showed an irreversibility of the contact angle change. There is therefore ongoing activity in order to find surface structures which favor reversibility of electrowetting under superhydrophobic conditions. Recently, Vrancken *et al.* designed a corrugated surface structure for which the transition from a Cassie–Baxter state with quasi-null hysteresis to a Wenzel state with liquid impalement stays reversible for maximum contact angles of 130°.[16]

Apart from this very recently reported case, up to now surfaces with a double texturation (micron-sized posts and nanotexturation) were proposed as the most promising solutions in order to obtain a robust Cassie state for a high resistance to impalement.[17–19] The work reported in this communication is a continuation of our previous work[20–22] on forests of nanowires, here extended on the preparation and wetting properties - including robustness upon external pressure - of double-scale micro-pillar nanowire surfaces. While silicon micropillars are prepared by the combination of optical lithography and silicon etching, the nanotexturation is obtained by silicon nanowire growth leading to unique wetting properties,[20] shown in Fig. 1. In order to compare the hierarchical integration of our specific nanoscale textured surfaces consisting of microscale pillar-like structures with nanowires on top, two types of superhydrophobic surfaces have been realized: micropillars (single-scale roughness) and micropillars covered by nanowires (micro/nano double-scale roughness) (Fig. 2 (a)–(d)). Different parameters such as pillar width, spacing and height, and height and density of nanowires layers have been investigated.

The comparison of the wetting properties of these surfaces is performed using electrowetting (EW) and drop impact experiments. In particular, we determine the robustness of the so-called 'Fakir' (Cassie–Baxter[2]) state against partial or total impalement.[23] Concerning the first method, after an EW cycle the variation of the contact angle (CA) is determined. We assumed that the Cassie state is maintained if a total CA reversibility is observed. Hence, the observation of irreversible behaviour during EW suggests that the liquid has partially or totally impaled the texture

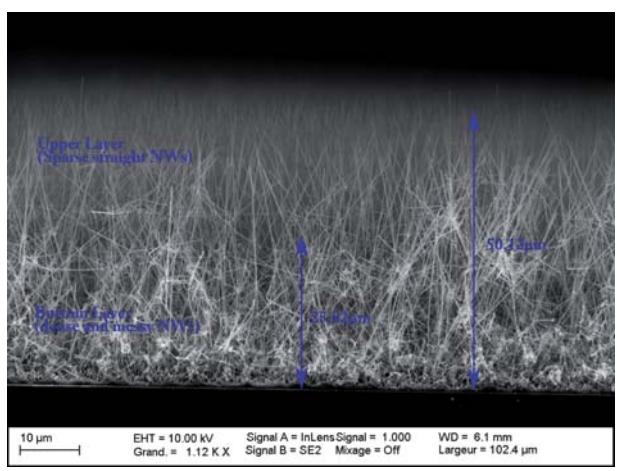

Fig. 1 SEM image of VLS Nanowire carpet coated with C_4F_8. The total height is about 50 µm. A double nanotexturation is observed: at the bottom, a dense and messy NW layer, on the top, sparse straight NW.

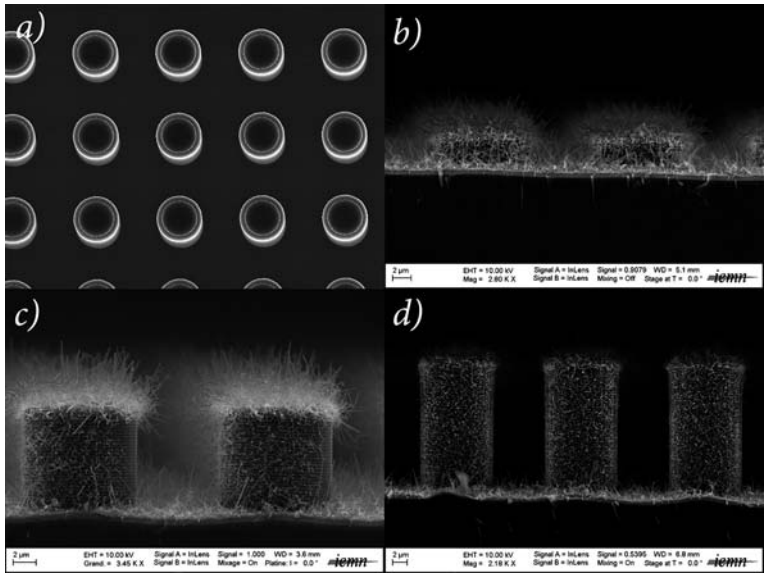

Fig. 2 SEM images of (a) pillar $P_5^{10}(20)$ (Top view), (b) $P_7^{10}(4)$ + NW-VLS2, (c) $P_7^{10}(10)$ + NW-VLS2, (d) $P_7^{10}(19)$ + NW-VLS2, all coated with C_4F_8.

(Wenzel state[3]). For the second method, we determined the impalement threshold, *i.e.*, the maximum drop velocity at impact, beyond which some liquid remains pinned on the surface.

Our experimental results show a correlation between the resistance to impalement for both EW and drop impact, and allows us to draw the following trends:

• Micropillar surfaces have a small impalement threshold and an irreversible EW behavior. Their weak performances make them inappropriate for droplet actuation by EW.

• As previously shown,[20–22] thick double-layered nanotextured surfaces both have a very high resistance impalement to drop impact, and a total reversibility during EW. These offer up to now one of the best performances available for robustness against liquid impalement. Otherwise surfaces made of a thinner layer of NWs are much less robust against impalement.[20,21]

• The double-scale surfaces resulting from a combination of short NWs and micropillars, and specifically investigated in this paper, provide a good performance under the condition that the geometrical parameters fulfil some requirements. More precisely the height of the micropillars has to be large enough and the space between the pillars has to be of the same order at the length of the NWs. A correlation between EW reversibility and drop impact impalement threshold is observed as well.

II. Surface preparation and characterization

1 Fabrication of silicon micropillars

Single-side polished silicon (100) oriented p-type wafers (Siltronix) (phosphorus-doped, 0.009–0.01 Ohm-cm resistivity) were used as substrate. The surface was first degreased in acetone and isopropanol, rinsed with Milli-Q water and then cleaned in a piranha solution (3 : 1 concentrated H_2SO_4/30% H_2O_2) for 15 min at 80 °C followed by extensive rinsing with Milli-Q water. A negative resist AZ$_n$LOF 2035 (Clariant, France) is spin-coated at 3000 rpm to create a 3.5 μm thick resin layer. A

ART ■ B925544C

softbake for 1 min on a hot plate at 90 °C is required in order to partially evaporate the solvent and hence to prevent adhesion of resin onto the mask. Then, exposure, post-exposure bake and development are conducted in order to transfer the mask patterns to the resist (latent image). Then, the silicon wafer was etched using Deep Reactive Ion Etching (DRIE), (Silicon Technology System) leading to high aspect ratio micro-pillars. We varied the etching time to obtain different heights of μ-pillars, *i.e.* 4, 10 and 19 μm.

2 Silicon nanowire (NWs) synthesis

The NWs were grown on Si/SiO_2 substrates using the vapour–liquid–solid (VLS) growth mechanism. Both the silicon surfaces and silicon surfaces featuring silicon μ-pillars are immersed in 50% hydrofluoric acid to remove the native oxide. Next, a SiO_2 layer (300 nm thick) is grown by Chemical Vapour Deposition (CVD). Finally, a gold layer (4 nm thick) is deposited by sputtering onto the Si/SiO_2 surface. The metallized interfaces are introduced in a CVD furnace chamber and heated at 500 °C under an SiH_4 flow. At this temperature, gold film dewetting leads to the formation of 10–100 nm diameter gold nanodroplets serving as catalysts for preferential silane decomposition. This decomposition leads to the formation of a liquid Au–Si eutectic. Oversaturation of these eutectic droplets by silicon atoms leads to the precipitation of Si and then to the formation of nuclei at the solid–liquid interface. After a certain time wires are obtained (elongation step) with the gold nanoparticle on top. Thus, the nanowire diameter is defined by the catalyst diameter, and the length is a function of time and pressure. All the samples have been prepared using 40 sccm of SiH_4 at 500 °C and a total pressure of 0.532 mbar during 60 min and 10 min for the VLS8 and VLS2 interfaces, respectively.[20–22] The protocols correspond to processes P1 (VLS2) and P2 (VLS8) in ref. 21. No doping reagent was used during the synthesis of nanowires.

3 Polymer plasma-based coating

A fluoropolymer (C_4F_8) was then deposited on the silicon nanowires and the silicon nanowires on the μ-pillar interfaces. The interfaces were placed onto a holder and then directly placed in the plasma chamber (Silicon Technology System) leading to a coverage of 30 nm thick of C_4F_8 [passivation gas, C_4F_8 (50 sccm); passivation time, 10 s] which is considered an insulator.

The polymer layer (C_4F_8) presents a contact angle of 105° and a hysteresis of 22° on a planar surface. We chose this polymer for a reason of uniformity between pillars and NWs: because the layer can be plasma-deposited, similarly to that used on NWs. The coating technique used by Bahadur *et al.*,[15] using a spin-coated Teflon polymer, offers a better hydrophobicity and a better resistance to impalement during EW, but cannot be applied on NWs as the spin-coating would damage them.

4 Surface characterization

Scanning electron microscopy (SEM) images were obtained using an electron microscope ULTRA 55 (Zeiss, France) equipped with a thermal field emission emitter and three different detectors (EsB detector with filter grid, high-efficiency In-lens SE detector, Everhart-Thornley secondary electron detector).

Table 1 summarizes the different surfaces we have realized. We characterize them with the notation $P^x{}_y(h)$ where P stands for pillar, x is its diameter, y its spacing and h its height. Fig. 2 shows a few representative cases. The basic setup consists of cylindrical posts, as shown in Fig. 2 (a). These pillars of variable size (see Table 1) are then covered with short NWs according to protocol VLS2 (Fig. 2 b–d). We have also produced surfaces with long NWs, grown on top of the pillars according to protocol VLS8 (not shown). On these surfaces the pillars, whose height is shorter than the height of long NWs, are completely shadowed by a forest of NWs so

Table 1 Contact angle, hysteresis and impalement degree after EW at 225 V_{TRMS}

P_x^y/h + C_4F_8	ϕ_s	r	θ_0^{theo} (°)	θ_0^{Exp} (°)	Hysteresis (°)	Impalement EW
$_2^4$(4)	0.35	2.74	141.3	—	25	160 − 98 = 62
$_2^{10}$(4)	0.54	2.09	128.9	—	35	160 − 99 = 61
$_5^{10}$(4)	0.35	1.69	141.3	—	23	158 − 97 = 61
$_7^{10}$(4)	0.27	1.54	150.9	—	19	162 − 84 = 78
$_2^4$(10)	0.35	4.49	141.3	145	23	160 − 122 = 38
$_5^{10}$(10)	0.54	3.18	128.9	134	24	161 − 108 = 53
$_7^{10}$(10)	0.35	2.39	141.3	137	26	160 − 102 = 58
$_2^4$(10)	0.27	2.08	150.9	148	19	160 − 106 = 54
$_2^4$(19)	0.35	7.98	141.3	145	23	153 − 97 = 56
$_2^{10}$(19)	0.54	5.36	128.9	144	24	158 − 96 = 62
$_5^{10}$(19)	0.35	3.79	141.3	146	26	161 − 94 = 67
$_7^{10}$(19)	0.27	3.17	150.9	151	19	161 − 85 = 76
NWs				160	0	see text

that a drop deposited on top of the surface merely sees the micro-scale modulations induced by pillars, see the discussion below.

III. Wetting and electrowetting experiments

1 Contact angle and hysteresis measurements

We performed contact angle and hysteresis measurements on each surface. For the contact angle measurement, a 3 μl deionised water droplet is deposited on each surface (pillar, pillar + NW) and a goniometer (GBX, France) determines each contact angle. The hysteresis was measured by spreading a 4 μl droplet on the surface (giving θ_a) and then sucking it (giving θ_r). The hysteresis is obtained from $\Delta\theta = \theta_a - \theta_r$, see Table 1. The impalement under EWOD is determined by the difference of the contact angle before and after applying the voltage. We observed that the contact angle evolved as a function of the surface fraction. The contact angle is observed to increase with the pillar spacing. Therefore, the hysteresis measurement showed the same trend; whatever the height of the pillar, $P_7^{10}(h)$ surfaces presented the lowest hysteresis (CAH = 19°). After the NW growth and the hydrophobic coating on each surface, the contact angle went up to 160° and the hysteresis to 0° ± 1°. Hence, this NW texturation on the micro-pillars leads to superhydrophobic surfaces with very low friction.

The contact angles measured on micro pillars surfaces are comparable to those obtained theoretically, see Table 1. To evaluate theoretically the CA, we assume that a drop deposited on the surface before EW, is in the Cassie state,[2]

$$\cos\theta_C^{theo} = \phi_s(1 + \cos\theta) - 1 \quad (1)$$

with ϕ_s as the surface fraction obtained for our cylindrical pillars,

$$\phi_s = \frac{\pi x^2}{4(x+y)^2} \quad (2)$$

We also calculated the roughness r of the pillar surfaces

$$r = 1 + \frac{\pi x h}{(x+y)^2} = 1 + \frac{4\phi_s h}{x} \quad (3)$$

2 EW experiments

In parallel, we carried out electrowetting experiments (EW) on each surface. The measurements are obtained in the following way: the voltage is applied between the drop and the substrate with a signal generator (CENTRAD GF 265, ELC, France), 0.5 to 21 V output at 1 kHz, coupled to a 50 dBm high-voltage amplifier (TEGAM, USA). This leads to a voltage range between 12.5 V to 250 V at amplifier output. A goniometer (GBX, France) was used to record and measure the CA during EW. To determine the reproducibility of the EW phenomenon, the following protocol is applied:

(1) Droplet formation on the surface (3 ± 0.1 μL) through a metallic, hydrophobic needle;

(2) A single voltage is applied (during 0.5 s) to the droplet through the same conductive needle at the beginning of the first EW cycle;

(3) Return to 0 V during 0.5 s (end of the first EW cycle);

(4) Steps 2 and 3 are repeated at least four times (EWOD cycle) at the same voltage in order to reach a stable value of CA.

These experiments constitute tests for the reversibility during EW, and reflect whether or not the liquid has changed from Cassie–Baxter to Wenzel states. EW allows for applying an external pressure to the liquid depending on some parameters as will be developed in *Section V - Discussion*.

3 EW on micropillars

Independently of the surface and the applied voltage (starting from 25 V_{TRMS}, the same phenomenon under EW is observed: from a contact angle around 160°, the applied voltage decreases the contact angle, which stays stuck at a constant value when the voltage is turned off (Fig. 3).

The variation of cosines of CA induced by EW *versus* squared voltage is plotted in Fig. 4 (a) for the four surfaces of pillar height equal to 19 μm. The trends for the two other surfaces (*i.e.*, 4 μm and 10 μm height) are similar: on the same surface, the higher the voltage, the larger the decrease of the CA, leading to a deeper impalement with a maximum CA variation of about 80° at 225 V_{TRMS}. The EW saturation

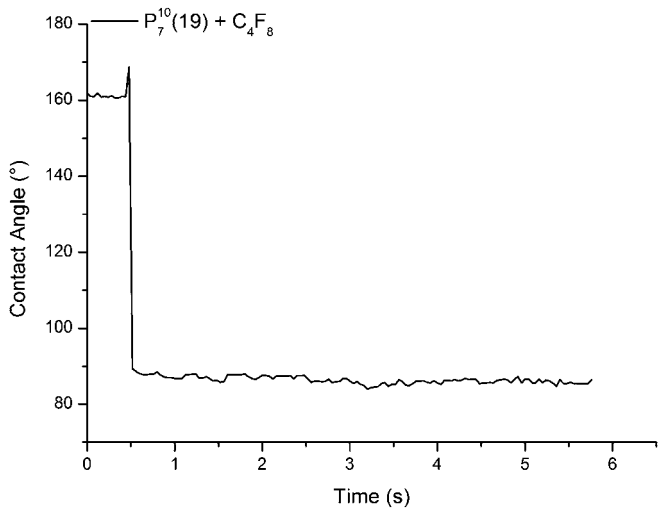

Fig. 3 Contact angle measurement during the EW cycle (at 225 V_{TRMS}) on $P_7^{10}(20) + C_4F_8$. It shows a complete irreversibility with EW, a transition from superhydrophobic to hydrophilic behaviour.

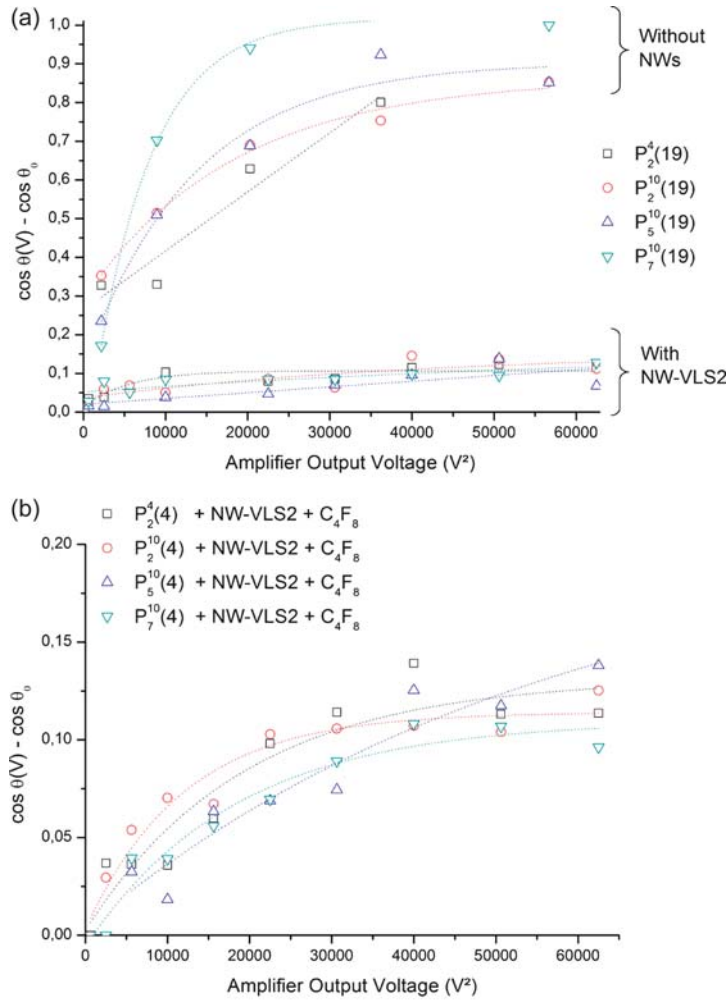

Fig. 4 Variation of the contact angle *versus* the squared voltage, after the first EW cycle, for different micro/nano double-scale roughness described by $P_x^y(h)$ + NW + C_4F_8 where P stands for pillar, x is its diameter, y its spacing and h its height.

appears at a voltage of about 140 V_{TRMS} with a maximum variation of the cosine between 0.7 and 1.0.

When comparing the different surfaces, no clear difference is seen at the same voltage. The level of impalement seems not to depend directly on the characteristics of the microstructures. EW on the microstructured surface leads to a transition from a superhydrophobic to a hydrophobic state (or hydrophilic in a few cases; below 90°). The droplet starts from a Cassie state, then moves to a Wenzel state once the voltage is on, and it never returns to the Cassie state when the voltage is turned off (*i.e.*, after the end of the first cycle).

4 EW on micropillars covered by nanowires

Different behaviours have been observed under EW according to the geometric properties of the corresponding surface.

In Fig. 4 (b) we compare the CA variation for the same height of micropillars (*i.e.* 19 μm) with and without nanowire structures, after the first application of the voltage. Here again, as for the surfaces with micropillars only, the trend is the same for the three heights of micropillars. While the cosine variation is between 0.7 and 1.0 for the pillars-only surfaces at 250 V_{TRMS}, this variation is inferior to 0.15 for the double-scale surfaces (micropillars covered by short NWs) at the same voltage. The saturation of EW appears at about 200 V_{TRMS} and no clear difference can be ascribed to the different double-scale surfaces after the first EW application. It is to be noted that, according to the measurement accuracy and to the strong heterogeneity of the surface, the error range of CA is about 6°.

To discriminate these surfaces through their robustness, we carried out CA measurements during more than four EW cycles. We performed 4 EW cycles on each surface, and compared their degree of reversibility. To quantify this degree, we defined CA_1, the CA during the first EW pulse and CA_2, the CA at the end of the EW cycle. CA_2–CA_1 represents the variation of CA after 4 EW cycles (Fig. 6) at 225 V_{TRMS}. In this particular case the difference of the reached values CA_1–CA_2 during an EW cycle depends on pillar height and on the surface fraction (Fig. 5). This CA difference quantifies the performance of the surface for droplet actuation, as it is related to the capillary force that can be induced by EW under reversible conditions.

- For short pillars $P_7^{10}(4)$ + NW-VLS2 + C_4F_8, the CA starts at 160° at 0 V, then decreases to $CA_1 = 146°$ when the voltage is prescribed (at 225 V_{TRMS}), and remained at this value whenever we turn the voltage off or on ($CA_1 = CA_2$). The CA variation is completely irreversible under EW.
- For intermediate pillars $P_7^{10}(10)$ + NW-VLS2 + C_4F_8, the CA starts at 158° at 0 V, then decreases to $CA_1 = 141°$ when the voltage is applied (at 225 V_{TRMS}) but goes back up to $CA_2 = 152°$ when the voltage is off. For each EW following cycle, the CA under EW is constant (CA = 141°) but after each relaxation (voltage turned off), the CA decreases until it reaches the CA after the first EW. After this first cycle, the drop seems to be in a partially impaled state. Depending on the roughness, the Wenzel state is reached after a variable number of EW cycles.

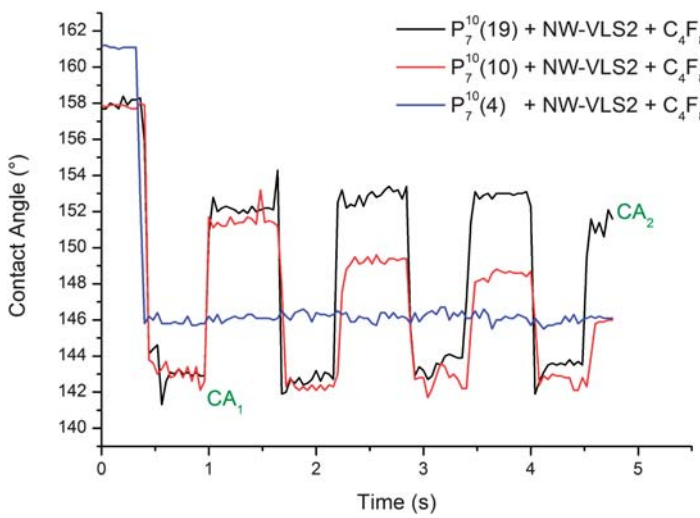

Fig. 5 Contact angle measurement during the EW cycle (at 225 V_{TRMS}) on the different micro/nano double-scale roughness. Notation characterizing the pillar geometry is as before. CA_1 corresponds to the contact angle during the first EW cycle, and CA_2 is the contact angle when the EW cycle is stopped.

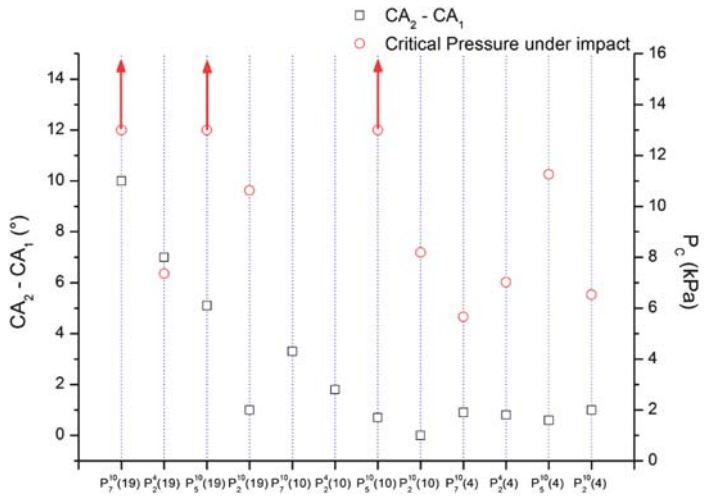

Fig. 6 CA_2–CA_1, the degree of reversibility for each surface (square symbols). It increases with the height and the space between the pillars. Comparison with the pressure threshold P_c for impalement obtained by drop impact (circles). The arrows denote that P_c is larger than 13 kPa for these specific surfaces.

• For tall pillars $P_7^{10}(19)$ + NW-VLS2 + C_4F_8, the CA starts at 158° at 0 voltage, then decreases to $CA_1 = 141°$ when the voltage is applied (at 225 V_{TRMS}) and rises up to $CA_2 = 152°$ when the voltage is off. Meanwhile, for each EW step, the CA relaxes to a permanent value. The surface stays in a semi-reversible state after the EW cycles.

While the NWs introduce a more robust superhydrophobic state on pillars without EW, the height of the pillars acts as a barrier to the total impalement of the droplet under EW: for the 4 μm short pillars + NWs, the Wenzel state is immediately obtained under EW; for the intermediate 10 μm pillars + NWs the CA shows a variation smaller than 5°, indicating that the liquid drop is deeply but partially impaled. Finally, the 19 μm pillars + NWs measurements seem to indicate that the drop is shallowly impaled, with about 10° of difference between CA_1 and CA_2. A comparison between the 10 μm and the 19 μm height pillars indicates that the P_7^{10} surfaces present the most important degree of reversibility. Furthermore, for these two height values, the quantity CA_1–CA_2 seems directly linked to the surface fraction ϕ_s: the P_7^{10} presents the smallest surface fraction, the CA variation under EW is the most important while the P_2^{10} has the largest surface fraction with a quasi-null CA variation under EW. This is consistent with the measurements obtained with the P_5^{10} and P_2^{10} surfaces which offer the same surface fraction: the degree of reversibility is approximately the same (*i.e.*, about 2° and 6° for the pillars with 10 μm and 19 μm height, respectively). Fig. 6 summarises all these results, together with the results of drop impact experiments described hereafter.

IV. Droplet impalement experiments

Description of the set-up

To carry out drop impact experiments, we used the same set-up as previously described,[21] which is shown in Fig. 7 (a). A sub-millimetric nozzle releases a drop of liquid (water/glycerin 50/50 mixture) from a height H that prescribes the impact velocity $U = (2gH)^{1/2}$ - which can be up to 4.7 m s^{-1}. The diameter of the drop is determined by the capillary length, and is well reproducible at $d = 2.6 \pm 0.1$ mm.

ART ■ B925544C

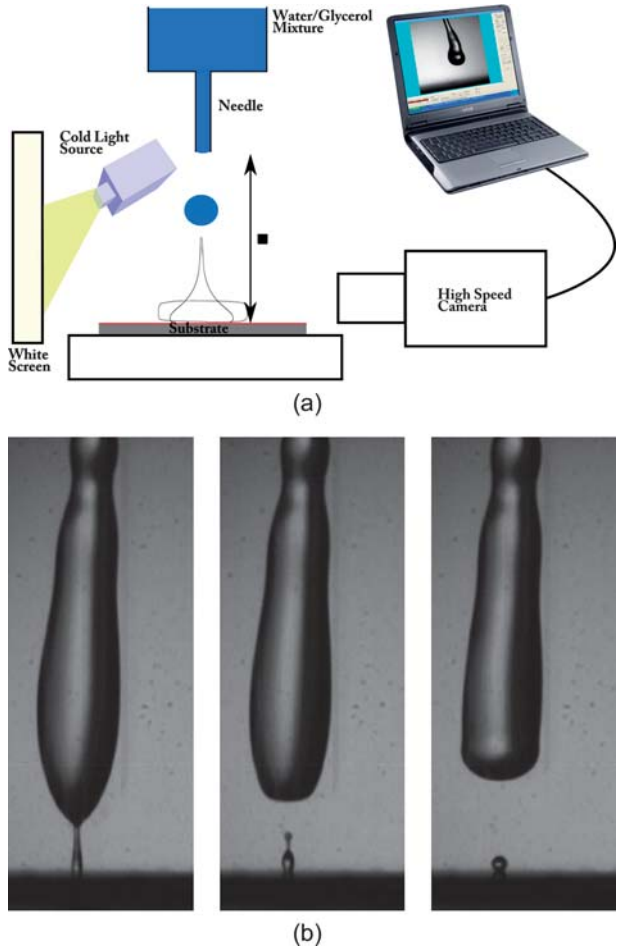

Fig. 7 (a) Experimental set-up, see text for details. (b) Typical snapshots from the high-speed camera, here showing a bouncing drop after impact and leaving an impaled tiny droplet at the impact location.

The physical parameters of the liquid are: kinematic viscosity $\nu = 6.2$ cSt, surface tension $\sigma = 0.066$ N m^{-1} and density $\rho = 1126$ kg m^{-3}. The mixture has a viscosity larger than water, which prevents both splashing - *i.e.*, the splitting of the main drop into tiny ones - and corrugations at the border of the drop during the spreading phase. Hence during the spreading and the retraction, the drop mostly remains axisymmetric. Using backlighting together with a high-speed camera (at a maximal rate of 8000 frames/s, with a resolution of 256 × 512), the shape of the interface during the spreading and bouncing processes can be determined. The magnification allows for an accuracy of about 8 μm per pixel.

To determine the pressure threshold for impalement, we determine the minimal height (or impact velocity) for which some liquid remains at the impact location. The height of fall H is increased until a sequence like in Fig. 7 (b) is observed, *i.e.*, some liquid in the form of a tiny droplet stays impaled at the centre of the impact location. This minimal height $H_{\min}$ gives the pressure threshold $P_c = \rho g H_{\min}$. Therefore, the key point to prevent the transition to Wenzel state as much as possible is to have the largest possible P_c. Our drop impact set-up allows for prescribing a dynamical pressure of $P_{\mathrm{dyn}} = \frac{1}{2}\rho U^2$ up to about 13 kPa.

It is noticeable that all pillar+long NWs surfaces (growth with VLS8 protocol, see section II.2 and Fig. 1) had threshold values much larger than the limit of 13 kPa. Actually, the length of NWs (about 40 μm) is much larger than the height of the micro-pillars, and it turns out that these surfaces have impalement properties that are very similar to those of the long NWs alone, without pillars. In this specific case, the micro-structure is shadowed by the NWs and has no influence.

Hence, in the aim for understanding the combined contribution of pillars and NWs on the robustness, it is more suitable to use the shorter NWs (Protocol VLS2) which height is comparable to or smaller than the height of the pillars. The short NWs of average height about 4 μm presented before, and represented in Fig. 2, are adapted to such a study. Therefore in what follows, we report only the quantitative results obtained for the surfaces of micro-pillars covered by the shorter NWs.

Previous existing results

Previous experiments have evidenced that droplet impact experiments are suitable for the determination of the impalement threshold on textured SH surfaces,[21,28–30] where the entry pressure is relatively large. By testing various surfaces textured by periodic arrays of micro-pillars, Reyssat *et al.* showed a relationship between geometrical properties of the texture and the impalement threshold [30] that can be written as:

$$P_c = \alpha \frac{\sigma h}{l^2} \tag{4}$$

where $\alpha \simeq 0.048$. The geometrical parameters h and l respectively stand for the height of the posts and the space between them. Therefore, the taller the pillars and the narrower the space between them, the better the robustness to impalement. They found the best robustness for $h = 26$ μm and $l = 3$ μm, corresponding to a dynamical pressure of $P_{dyn} = 4.5$ kPa.[30]

At almost the same time, Bartolo *et al.* carried out the same type of experiments.[29] Although less exhaustive than ref. 30 and with less robust surfaces, their results evidenced two important points: (1) the pillar height h ceases to have a noticeable influence on robustness beyond a certain limit (in their experiments, the robustness was not improved by an increase of h above about 25 μm); (2) by comparing the impalement pressure in both impact and (static) evaporation experiments, the authors concluded that hydrodynamic forces do not play any significant role in the impalement transition. Therefore, the pressure threshold is the same whether it is prescribed dynamically by drop impact, or statically by other means like evaporation, drop squeezing or electrowetting.

Based on these quantitative results on micro-pillars, it is straightforward that a much better robustness would be obtained by using a much smaller, rougher and denser texture. One of our recent studies[21] showed that a dense array of silicon nanowires, coated with an ad-hoc chemical, was robust enough to prevent liquid impalement. Our best surfaces were covered with long NWs that form a lower dense and entangled structure and an upper looser but more regular structure (see Fig. 1), had an impalement threshold P_c larger than 17 kPa.

Our results on multi-scale textured surfaces

We tested various surfaces for their robustness on drop impact impalement, and compared them with potential reversibility during EW. The results are presented in Table 2, and plotted in Fig. 6 in comparison with EW experiments. Due to the limited height of fall in our laboratory it was not possible to measure the exact threshold for some of the surfaces as they were too robust. In this case we indicate

Table 2 Impalement thresholds in drop impact for various double-scale substrates. P_c^* is the pressure that would be found for substrates made only of micro-pillars, according to the results of ref. 30, see eqn (4)

Pillar height (μm)	Pillar width (μm)	Interspace (μm)	P_c (kPa)	P_c^* (kPa)
4	4	2	7.025	1.41
4	10	2	6.53	1.41
4	10	5	11.264	0.225
4	10	7	5.66	0.115
10	10	2	8.19	3.52
10	10	5	≥13	0.562
19	4	2	7.36	6.68
19	10	2	10.62	6.68
19	10	5	≥13	1.07
19	10	7	≥13	0.545
No pillar, only NWs	—	—	7.14	0

that the threshold is larger than the maximal accessible dynamical pressure of 13 kPa.

By comparing the different results, it turns out that:

• in comparison to micro-pillars surfaces tested in ref. 30, the adjunction of NWs increases significantly the robustness against impalement as quantified by P_c;

• in comparison to surfaces with short NWs only, the combination of pillars and NWs can both significantly increase or decrease P_c. The double-scale seems to get its best efficiency when micro-pillars are much taller than the height of the NWs and when the pillar interspace is comparable to NWs height: here, a spacing of 5 μm with NWs of height 4 μm gave the best results.

Therefore, a double-scale structure is not necessarily a guarantee for robustness. One has to take into account the length ratio between micro- and nano-scale elementary units. To some extend, the threshold P_c can be related to the degree of reversibility CA_2–CA_1 (see Fig. 6), except for P_2^4(19) and P_5^{10}(4) surfaces.

V. Discussion

The performance of the droplet actuation by EW on a double-textured (micro/nano) surface depends on two parameters: the roughness r (mostly dependent on the height of the micro-structuration) and the surface fraction ϕ_s. The total impalement of the liquid inside the pillars is prevented only by the surfaces with the tallest micropillars. As far as it is concerned, the surface fraction can be ascribed to the reversibility of the CA (we have called it degree of reversibility under EW cycles). In other words the transition to the Wenzel state is prevented by the height of the pillars. Once this vertical impalement is limited, a shallower impalement ('quasi-Cassie state') is promoted by a decrease of the surface fraction, and by a space between pillars of the same order as the length of the nano-textutation.

To sum up the previous results, and put them in a broader and more fundamental perspective, we comparatively evaluate the liquid impalement in the texture *via* a prescribed pressure within two configurations:

• The impact of a droplet. In this case, we have a *dynamical* pressure due to the initial kinetic energy of the drop, which equals $P_{dyn} = \frac{1}{2}\rho U^2$, where U is the impact velocity;

• The deformation of the droplet in the vicinity of the contact-line induced by EW.

In this latter case, the pressure is due to the strong local curvature that builds up close to the contact-line. The Laplace pressure P_L balances the Maxwell stress due to the accumulation of charges near the contact-line, as shown by Mugele and Bührle.[24,25] More precisely, under the action of EW the drop *apparent* contact-angle θ_{app} is modified down to a certain scale λ. The apparent contact angle is given by the Young–Lippman eqn (8):

$$\cos(\theta_{app}) = \cos(\theta_0) + \frac{1}{2\sigma}\frac{\varepsilon_0 \varepsilon V^2}{\lambda} \quad (5)$$

where V stands for the applied voltage, ε_0 stands for the permittivity of the vacuum and ε stands for the relative effective permittivity of the surface dielectric.

However, accurate visualizations evidenced that the contact angle *always* converges towards the Young's contact-angle - *i.e.*, the angle θ_0 in the absence of voltage - at a distance from the contact-line smaller than λ.[24] The length λ corresponds to an effective width of the dielectric, as shown in Figures 10 and 11 of ref. 24. Another direct evidence of this phenomenon was reported in a still unpublished paper,[26] where it was shown by reflection microscopy that the impalement first starts at the contact-line.

Therefore, the local slope of the drop evolves from the apparent (macroscopic) contact-angle given by eqn (5) to the microscopic contact-angle within a distance of λ. For textured surfaces, the microscopic angle is the Cassie–Baxter angle if the liquid has not impaled the texture yet.

To check Mugele and Bührle's observations on our surfaces, we acquired magnified images of a drop during electrowetting at the vicinity of the contact line. Fig. 8

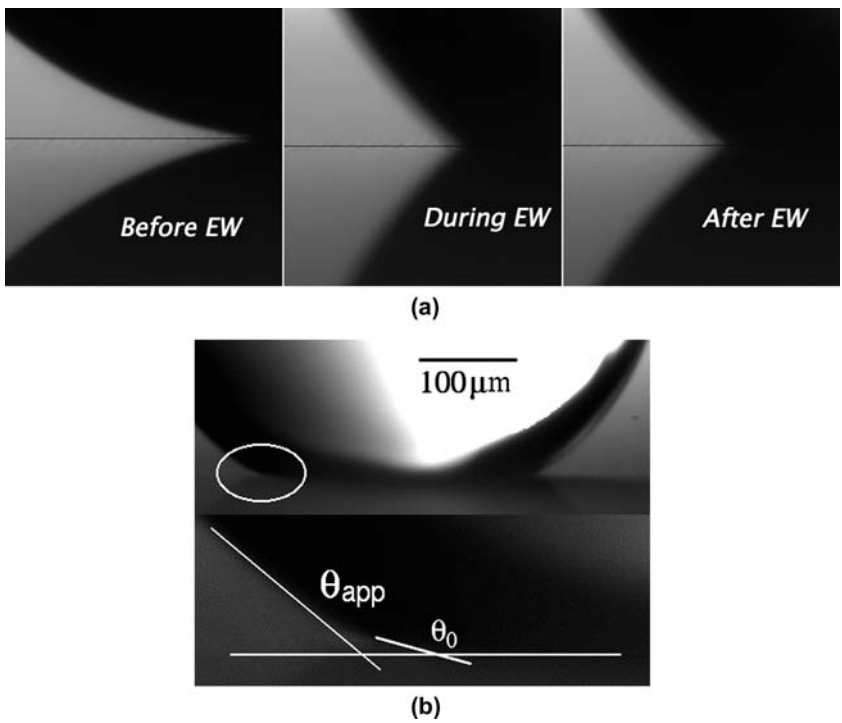

Fig. 8 Magnified view of the vicinity of the contact-line (a) For a substrate showing irreversibility (impalement) before, during and after electrowetting. (b) For a totally reversible substrate with higher NWs, showing a transition from apparent θ_{app} to Cassie–Baxter θ_0 angle close to the contact-line.

(a) represents three images before, during and after EW for a surface where liquid is impaled during EW. It turns out that the 'quality' of the surface, *i.e.* its resistance under EW or drop impact impalement, is visible close to the contact-line. When the liquid is impaled during EW (Fig. 8 (a)), the drop profile shows a unique slope. This is understandable considering that, as the liquid has impaled the surface, it leads to a drastic decrease of the effective thickness of dielectric λ. On the contrary, if the liquid stays shallow and does not enter significantly into the texture, we clearly see a transition from the macroscopic Lippmann (apparent) angle to the Cassie–Baxter angle θ_0 close to the contact-line (Fig. 8 (b) and magnified view therein). This is a direct evidence that the effective thickness of dielectric λ is large enough to be observed. We estimated it to about 35 μm from this picture. Again, this is consistent with Mugele's observations of a water drop immersed in oil on flat, non-textured surfaces. Here this is the first time that it was directly observed on a textured surface in ambient air.

The local Gaussian curvature is given by the secondary derivative of the drop profile $r(z)$, with z standing for the vertical coordinate. If λ is small enough, one can approximate the second derivative by the finite difference of first derivatives. Therefore, the Laplace pressure close to the contact-line equals

$$P_{\mathrm{L}} = \sigma\kappa \simeq \sigma\left(\frac{\mathrm{d}^2 r}{\mathrm{d}z^2}\right)_{z=\lambda} \simeq \frac{\left(\frac{\mathrm{d}r}{\mathrm{d}z}\right)_{z=\lambda} - \left(\frac{\mathrm{d}r}{\mathrm{d}z}\right)_{z=0}}{\lambda} \tag{6}$$

The derivatives $\frac{\mathrm{d}r}{\mathrm{d}z}$ are related to the apparent and Cassie–Baxter angles, leading to the following expression

$$\kappa = \frac{1}{\lambda}\Big(\cot\big(\theta_{\mathrm{app}}\big) - \cot\big(\theta_0\big)\Big) \tag{7}$$

From eqn (7) and after a bit of algebra, we obtain the expression

$$P_{\mathrm{L}} = \sigma\kappa = \frac{\sigma}{\lambda}\left(\frac{\frac{\varepsilon_0\varepsilon}{2\sigma\lambda}V^2 + \cos(\theta_0)}{\sqrt{1 - \left(\frac{\varepsilon_0\varepsilon}{2\sigma\lambda}V^2 + \cos(\theta_0)^2\right)}} - \cot(\theta_0)\right) \tag{8}$$

The Laplace pressure *versus* voltage V obtained from eqn (8) is plotted in Fig. 9 for three different values of dielectric thickness λ. From these plots, it is clear why impalement occurs at low voltage on surfaces with short NWs, as the pressure induced by EW reaches rapidly a few tens of kPa (which is far beyond the measured impalement threshold, see Table 2). Not only are short NWs intrinsically less resistant to impalement (as evidenced by drop impact experiments (21)), but also their thin layer of dielectric produces a larger pressure for the same CA difference. Hence, for the same actuation force under EW, which is quantified by the difference $\cos(\theta_{\mathrm{app}}) - \cos(\theta_0)$, taller NWs like those produced by the VLS8 protocol have to support a smaller pressure due to the larger effective thickness of dielectric (see eqn (7)). Once the liquid has not impaled, this large effective thickness is preserved.

To conclude, we explained why the height of the pillars and that of NWs are essential to prevent irreversible behaviour under EW. For double-scale surfaces, tall pillars associated with shorter NWs are optimal if the space between pillars l is comparable to the height of the NWs.

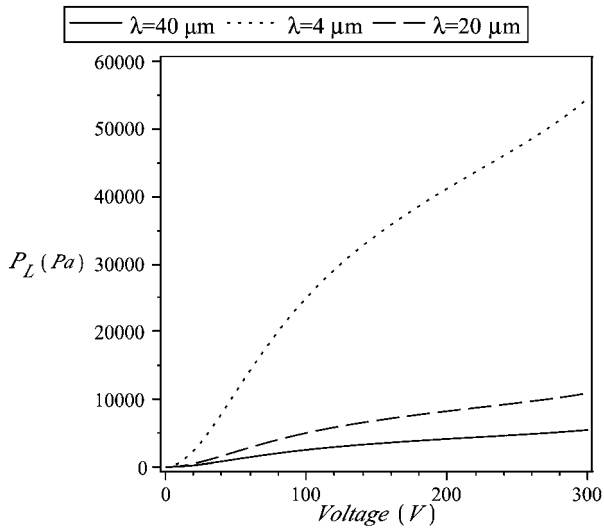

Fig. 9 Pressure induced by electrowetting, resulting from the equilibrium between the Maxwell stress and capillary forces.

References

1 N. K. Adam, *The Physics and Chemistry of Surfaces*, 1 st Ed. (Oxford Clarendon), 180–181 (1930).
2 A. Cassie and S. Baxter, *Trans. Faraday Soc.*, 1944, **40**, 546.
3 R. Wenzel, *Ind. Eng. Chem.*, 1936, **28**, 988.
4 R. Blossey, *Nat. Mater.*, 2003, **2**, 301.
5 Z. Burton and B. Bushan, *Nano Lett.*, 2005, **5**, 1607.
6 R. Fair, *Microfluid. Nanofluid.*, 2007, **3**, 245.
7 J. Heikenfeld and M. Dhindsa, *J. Adhes. Sci. Technol.*, 2008, **22**, 319.
8 G. Lippmann, *Ann. Chim. Phys.*, 1875, **5**, 494.
9 B. Berge and J. Peseux, *Eur. Phys. J. E*, 2000, **3**, 159.
10 R. A. Hayes and B. J. Feenstra, *Nature*, 2003, **425**, 383.
11 F. Mugele and J.-C. Baret, *J. Phys.: Condens. Matter*, 2005, **17**, R705.
12 A. Torkkeli2003.
13 D. L. Herbertson, C. R. Evans, N. J. Shirtcliffe, G. McHale and M. I. Newton, *Sens. Actuators, A*, 2006, **130–131**, 189.
14 N. Verplanck, Y. Coffinier, V. Thomy and R. Boukherroub, *Nanoscale Res. Lett.*, 2007, **2**, 577.
15 V. Bahadur and S. V. Garimella, *Langmuir*, 2008, **24**, 8338.
16 R. J. Vrancken and et al, *Langmuir*, 2009, to appear.
17 N. A. Patankar, *Langmuir*, 2004, **20**, 8209.
18 Y. Kwon, N. A. Patankar, J. Choi and J. Lee, *Langmuir*, 2009, **25**, 6129.
19 Y. C. Jung and B. Bhushan, *Langmuir*, 2009, Articles ASAP.
20 N. Verplanck, E. Galopin, J.-C. Camart, V. Thomy, Y. Coffinier and R. Boukherroub, *Nano Lett.*, 2007, **7**, 813.
21 P. Brunet, F. Lapierre, V. Thomy, Y. Coffinier and R. Boukherroub, *Langmuir*, 2008, **24**, 11203.
22 F. Lapierre, V. Thomy, Y. Coffinier., R. Blossey and R. Boukherroub, *Langmuir*, 2009, **25**, 6551.
23 S. Moulinet and D. Bartolo, *Eur. Phys. J. E*, 2007, **24**, 251.
24 F. Mugele and J. Buehrle, *J. Phys.: Condens. Matter*, 2007, **19**, 375112.
25 F. Mugele, *Soft Matter*, 2009, **5**, 3377–3384.
26 A. Staicu, , G. Manukyan and and F. Mugele, arXiv:0801.2683v1, 2008.
27 D. Quéré, *Rep. Prog. Phys.*, 2005, **68**, 2495.
28 K. K. S. Lau and et al, *Nano Lett.*, 2003, **3**, 1701.
29 D. Bartolo and et al, *Europhys. Lett.*, 2006, **74**, 299.
30 M. Reyssat and et al, *Europhys. Lett.*, 2006, **74**, 306.